

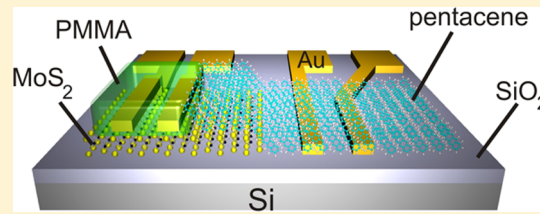
Hybrid, Gate-Tunable, van der Waals p–n Heterojunctions from Pentacene and MoS₂

Deep Jariwala,[†] Sarah L. Howell,[†] Kan-Sheng Chen,[†] Junmo Kang,[†] Vinod K. Sangwan,[†] Stephen A. Filippone,[†] Riccardo Turrisi,[‡] Tobin J. Marks,^{*,†,‡} Lincoln J. Lauhon,^{*,†} and Mark C. Hersam^{*,†,‡}

[†]Department of Materials Science and Engineering and [‡]Department of Chemistry, Northwestern University, Evanston, Illinois 60208, United States

Supporting Information

ABSTRACT: The recent emergence of a wide variety of two-dimensional (2D) materials has created new opportunities for device concepts and applications. In particular, the availability of semiconducting transition metal dichalcogenides, in addition to semimetallic graphene and insulating boron nitride, has enabled the fabrication of “all 2D” van der Waals heterostructure devices. Furthermore, the concept of van der Waals heterostructures has the potential to be significantly broadened beyond layered solids. For example, molecular and polymeric organic solids, whose surface atoms possess saturated bonds, are also known to interact via van der Waals forces and thus offer an alternative for scalable integration with 2D materials. Here, we demonstrate the integration of an organic small molecule p-type semiconductor, pentacene, with a 2D n-type semiconductor, MoS₂. The resulting p–n heterojunction is gate-tunable and shows asymmetric control over the antiambipolar transfer characteristic. In addition, the pentacene/MoS₂ heterojunction exhibits a photovoltaic effect attributable to type II band alignment, which suggests that MoS₂ can function as an acceptor in hybrid solar cells.



KEYWORDS: Organic, transition metal dichalcogenide, gate-tunable, antiambipolar, photovoltaic

The isolation of layered materials as passivated, dangling bond-free monolayers presents a unique platform for integration in previously unexplored device structures.^{1,2} For instance, semimetallic graphene, insulating boron nitride, and semiconducting MoS₂ have been stacked together to yield atomically thin memory devices, photodetectors, and field-effect transistors.^{3–6} This principle has also been exploited to fabricate heterojunctions between conventional silicon and 2D materials^{7–9} as well as carbon nanotubes with 2D materials¹⁰ and amorphous oxide semiconductors.¹¹ Similarly, organic molecular and polymer semiconductors are free of dangling bonds and native surface oxides, which suggests new opportunities for van der Waals heterostructures. Despite this potential, the integration of organic semiconductors with 2D materials has thus far been limited primarily to templating ordered film growth to improve the performance of the channel or contacts in conventional field-effect transistor (FET) geometries.^{12–16} Due to their relatively large light capture cross sections, organic semiconductors also hold promise for enhancing the performance of photovoltaics based on 2D materials. Although some preliminary studies have appeared in this regard,^{17,18} a clear understanding of charge transport across the interface between organic and 2D semiconductors is lacking.

In an effort to better understand and exploit the potential of van der Waals heterostructures between organic and 2D semiconductors, we explore here the electronic and optoelectronic response in p–n heterojunctions based on pentacene and

MoS₂. The operating principles and band profiles of this system are characterized by direct charge transport measurements, scanning photocurrent microscopy, electrostatic force microscopy, and finite element modeling. This comprehensive experimental and computational study reveals that pentacene forms a type-II heterojunction with MoS₂, which yields asymmetric antiambipolar transfer curves when operated as a three-terminal, gate-tunable diode. Furthermore, these p–n heterojunctions possess a clear photovoltaic response upon optical irradiation, which suggests that MoS₂ can function as an acceptor in hybrid solar cells.

Devices were fabricated from mechanically exfoliated MoS₂ flakes. Electron beam lithography was used to define the electrodes and junction area. Pentacene films were then deposited via thermal evaporation. We have fabricated >10 devices in total, and show qualitatively similar behavior. Results from two representative devices (2L MoS₂/40 nm pentacene) are shown in the figures. The resulting four-electrode test structure consists of a MoS₂ FET, pentacene/MoS₂ heterojunction, and a pentacene FET in series (representative device in Figure 1a, from left to right). The heterojunction region lies within the rectangular opening in the PMMA film (Figure 1b),

Received: October 11, 2015

Revised: November 28, 2015

Published: December 10, 2015

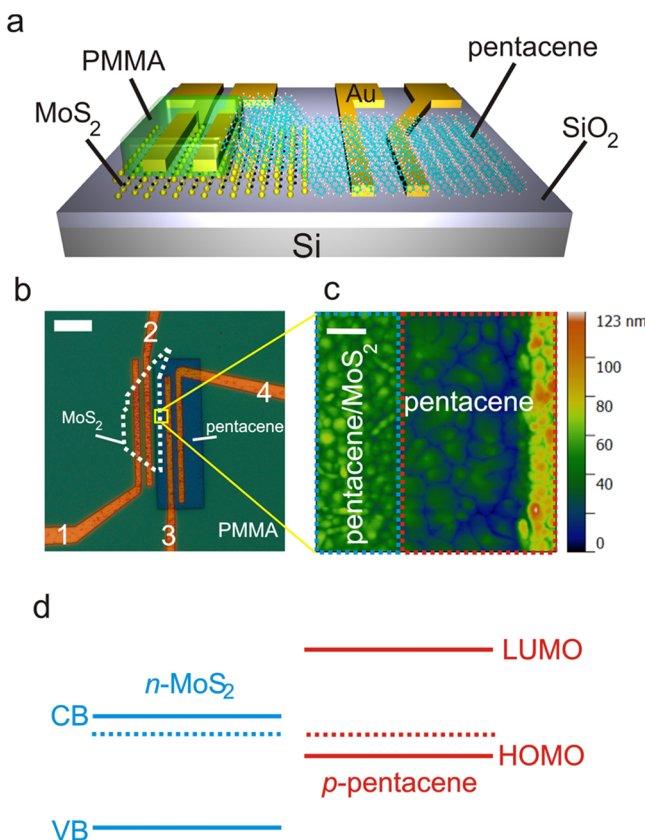


Figure 1. Structure of the pentacene/MoS₂ p–n heterojunction. (a) Three-dimensional device schematic. Most of the MoS₂ flake and electrodes are covered with PMMA to avoid shorting of electrodes by the thermally evaporated pentacene. (b) Optical micrograph of a representative MoS₂/40 nm pentacene device. The MoS₂ flake boundary is indicated by the white dashed line. The darker colored rectangle is an opening in the PMMA that exposes the gold pentacene bottom electrodes and a portion of the MoS₂ flake (scale bar = 10 μ m). Electrodes 1–2 define an n-type MoS₂ FET, 3–4 define a p-type pentacene FET, and 2–3 define the p–n heterojunction device. (c) AFM topography image of the junction area indicated by the yellow square in b. The pentacene grain size is smaller on MoS₂ compared to the surrounding SiO₂ substrate. The increased height at the right edge corresponds to the Au electrode below the 40 nm thick pentacene layer (scale bar = 500 nm). (d) Band alignments between ultrathin MoS₂ and pentacene showing the conduction band (CB) and valence band (VB) for MoS₂ and the highest occupied and lowest unoccupied molecular orbital (HOMO and LUMO) levels for pentacene.

which defines a partially overlapping region of a MoS₂ flake and the pentacene film (Figure 1a–b). This geometry of partially overlapping semiconductors allows direct and separate probing of the contact and heterojunction interfaces with scanning probe techniques while simultaneously applying a gate voltage, which is not possible in a truly vertical device geometry. In atomic force microscopy (AFM) topography imaging (Figure 1c), the abrupt change in the pentacene film grain size coincides with the boundary with the underlying MoS₂. Because pentacene and MoS₂ have complementary p-type and n-type doping with electron affinities of 2.5 eV¹⁹ and 4.2 eV (bilayer),^{20,21} respectively, and optical band gaps \geq 1.9 eV, the band alignment at the pentacene/MoS₂ heterojunction is expected to be type II as shown in Figure 1d.

The type II alignment results in a built-in potential and rectifying I_D – V_D characteristics. Figure 2a shows a three-dimensional

surface plot of the I_D – V_D (output) characteristics at different V_G values. For the pentacene/MoS₂ heterojunction, V_D refers to the bias on the pentacene electrode (electrode 3 in Figure 1b) such that $V_D > 0$ corresponds to forward bias, while the MoS₂ electrode (electrode 2 in Figure 1b) is grounded. The heterojunction transitions from a nearly insulating state at either extremes of the V_G range ($V_G = 60$ V and $V_G = -80$ V) to a highly rectifying output behavior at intermediate values. The transfer plots in Figure 2b further demonstrate the gate-tunability of the current through the p–n heterojunction. The transfer curve of the heterojunction (green) shows an antiambipolar response, which has also been observed in 1D–2D CNT–MoS₂,¹⁰ 2D–2D MoS₂–WSe₂,^{22,23} and 1D–3D CNT–IGZO¹¹ p–n heterojunctions. In contrast to these earlier devices in which the transfer characteristics are symmetric, the pentacene/MoS₂ heterojunction transfer characteristics are asymmetric with different slopes (i.e., transconductances) on either side of the I_D peak (see Supporting Information Section S2 for more details). Asymmetry in the antiambipolar transfer characteristic presents potential advantages in emerging circuit applications¹¹ and could be harnessed to achieve simultaneous phase¹¹ and amplitude²⁴ shift keying for wireless telecommunication technologies.

To identify the origin of the observed transconductance asymmetry, finite element simulations were performed (using Sentaurus TCAD) that numerically solve the Poisson and continuity equations governing free carrier transport. Where available, materials parameters were taken from the literature.^{20,21} The remaining parameters (e.g., mobility and trap concentrations) used in the heterojunction device model (Figure 2d) were informed by first modeling the unipolar FETs (Figure 2c) on either side of the p–n heterojunction (see Supporting Information Section S4, Table S1, S2 for more details). Our model assumes the pentacene material assembled on MoS₂ has the same material parameters (e.g., doping, mobility, etc.) as that assembled on SiO₂, although minor changes in substrate roughness and type can influence the molecular assembly of the overlying pentacene.^{16,25,26} We find that increasing (decreasing) the ratio of the MoS₂ to pentacene mobility (Figure 2e) or channel length (Figure 2f) leads to a left (right) and right (left) leaning antiambipolar asymmetry, respectively. In other words, the antiambipolar asymmetry can be controlled by the ratio of the series resistances of the two semiconductor channels. The electrostatic force microscopy (EFM) measurements discussed below support this interpretation that the dominating resistances of the channels govern the current flow in forward bias and thus influence the asymmetry of the antiambipolar response.

The type II alignment of the pentacene/MoS₂ heterojunction suggests that MoS₂ can act as an acceptor in a photovoltaic cell. Figure 3 shows I_D – V_D curves in the dark and when the pentacene/MoS₂ heterojunction is illuminated. As expected for a type II heterojunction, a photovoltaic effect is observed upon illumination with an open circuit voltage $V_{OC} \sim 0.3$ V and a short circuit current $-I_{SC} \sim 3$ nA. We observe that I_{SC} steadily increases with decreasing gate bias while the V_{OC} remains nearly constant as a function of V_G (Figure 3b–c). The relative insensitivity of V_{OC} to V_G has been observed previously in MoS₂–WSe₂ junctions²² and is attributed to the shared gate causing minimal net separation between the Fermi levels on either side of the heterojunction. The spectral response of I_{SC} exhibits a peak between excitation wavelengths of 600 and 650 nm (Figure 3d), which is consistent with the optical absorption

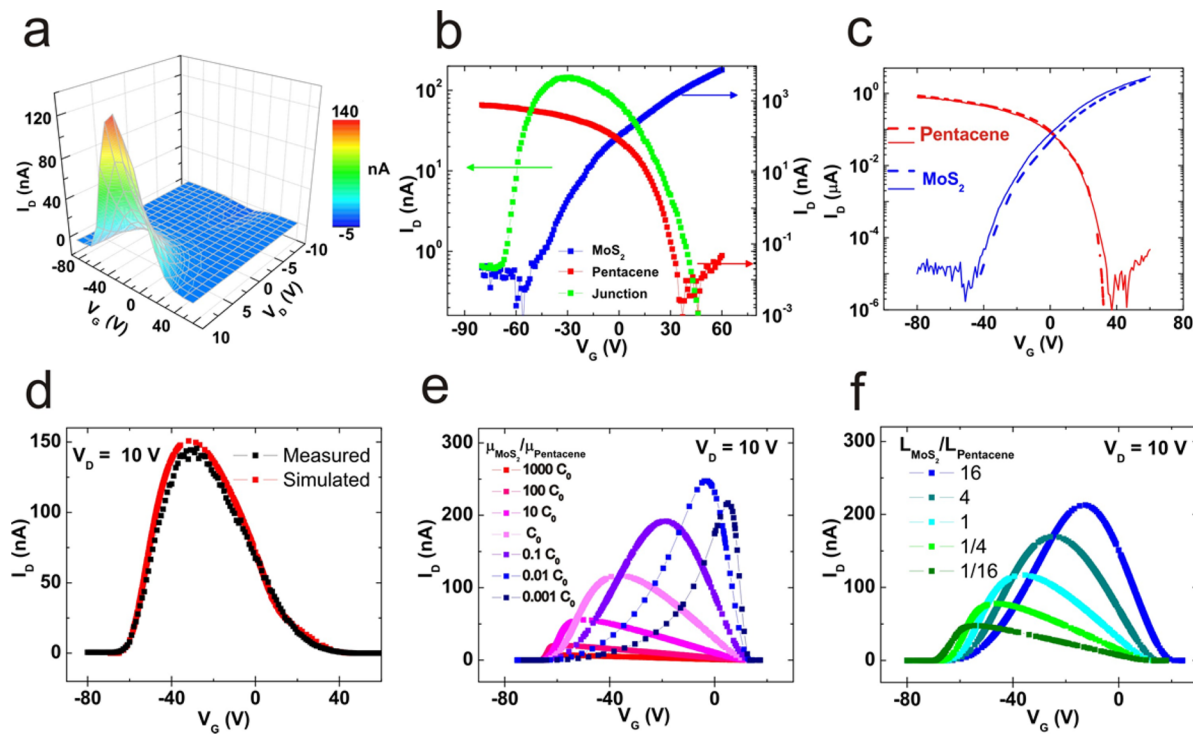


Figure 2. Electrical properties of the pentacene/MoS₂ antiambipolar p–n heterojunctions. (a) Gate-dependent I_D – V_D (output) characteristics of a representative device. The large current under forward bias and negligible current under reverse bias demonstrate the rectifying nature of the junction. (b) Semilog transfer characteristics of the pentacene (red, $V_D = 10$ V) and MoS₂ (blue, $V_D = 1$ V) FETs as well as the junction (green, $V_D = 10$ V). The junction transfer curve shows an asymmetric antiambipolar characteristic. (c) Simulated (dashed lines) and experimental (solid lines) transfer characteristics of pentacene (red) and MoS₂ (blue) FETs with measured field-effect mobilities of 0.004 and $1.7 \text{ cm}^2/\text{V}\cdot\text{s}$. (d) Simulated antiambipolar transfer plot of the junction (red) along with the measured transfer characteristic (black). Simulated junction transfer characteristics showing the tuning of the antiambipolar asymmetry by varying (e) ratio of the MoS₂ to pentacene mobility values and (f) nonoverlapped channel lengths. The product of the varied quantity (μ or L) is held constant, where the proportionality constant C_0 is the ratio of the mobilities for the device in d.

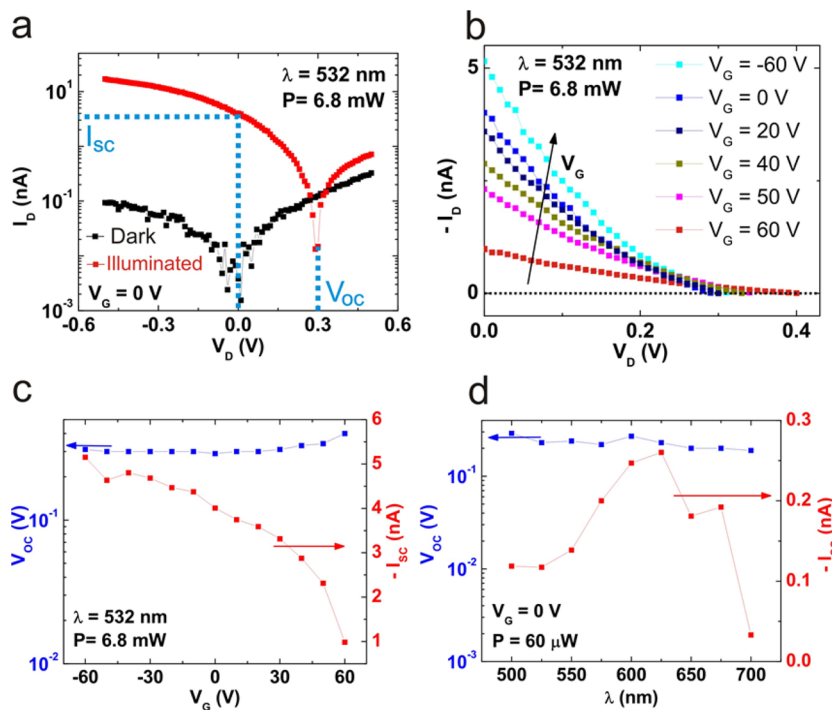


Figure 3. Photovoltaic effect in pentacene/MoS₂ p–n heterojunctions. (a) Dark (black) and illuminated (red) semilog I_D – V_D characteristics of the junction at $V_G = 0$ V (irradiation spot size is $1\text{--}2 \mu\text{m}$ and is centered on the edge of the overlapped pentacene/MoS₂ region). A photovoltaic effect with a $V_{OC} = 0.3$ V and $I_{SC} = -3$ nA is observed. (b) Illuminated I_D – V_D characteristics of the junction at varying gate biases. The area under the curve increases with decreasing V_G value. The arrow indicates V_G transitioning from positive to negative values. (c) Gate dependence of V_{OC} and I_{SC} showing constant V_{OC} while I_{SC} steadily increases with decreasing V_G . (d) Spectral dependence of V_{OC} and I_{SC} as a function of incident wavelength.

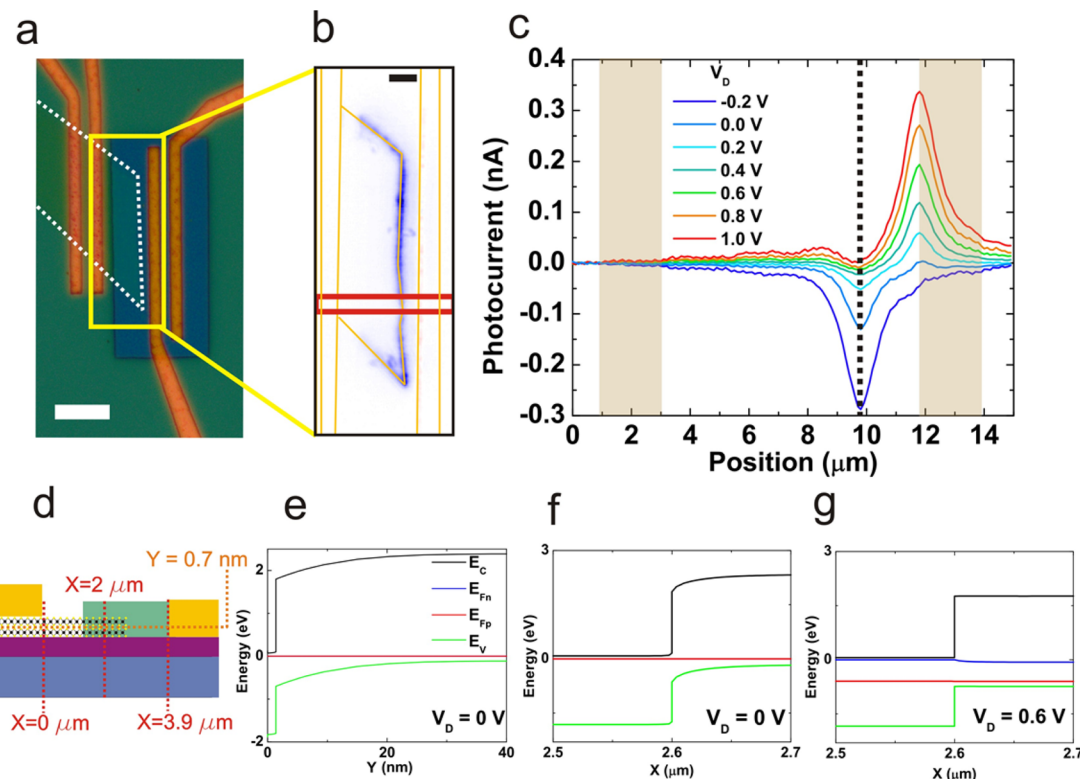


Figure 4. Spatial and bias dependence of photocurrent. (a) Optical micrograph of a representative device (2L MoS₂, 40 nm pentacene) that was scanned under a laser beam (scale bar = 10 μm). (b) Spatial photocurrent map at $V_D = 0$ V of the region indicated by the yellow rectangle in the optical micrograph. The largest photocurrent (blue region) is observed at the edge of the MoS₂ flake, while there is negligible photocurrent response from the contacts on either side of the junction (scale bar = 3 μm). (c) Photocurrent line profiles averaged over the red rectangle shown in b at varying V_D values. The gold rectangles indicate the position of the electrodes, while the black dashed line indicates the end of the overlapped pentacene/MoS₂ region. (d) Schematic diagram of the simulated junction device geometry. (e) Band profiles at $V_D = 0$ V across a vertical cross section of the junction at $X = 2 \mu\text{m}$ indicating the presence of an electric field normal to the interface. (f) Horizontal band profiles near the edge of the overlapped pentacene/MoS₂ region ($X = 2.6 \mu\text{m}$). (g) Band alignments in a horizontal cross-section at the flat band condition ($V_D = 0.6$ V). E_c and E_v represent conduction and valence band energies, respectively, while E_{Fn} and E_{Fp} represent quasi-Fermi levels for electrons and holes, respectively.

profile of pentacene. Since both pentacene (see absorption spectrum in Supporting Information Section S1) and MoS₂ absorb in the same range and have similar absorption coefficients,^{27,28} the thicker pentacene layer is estimated to absorb at least 20 times more light than MoS₂ in these devices. The power conversion efficiencies are rather low (~0.004% at 625 nm) as a result of the suboptimal photocurrent collection efficiency in the lateral device geometry.

Scanning photocurrent microscopy (SPCM) and modeling are next employed to further explore the photovoltaic performance of the pentacene/MoS₂ heterojunction. During SPCM, a diffraction-limited laser beam is scanned over the device, while the current or voltage is recorded as a function of position. Figure 4a shows an optical micrograph of a representative device where the yellow outlined box highlights the area that was interrogated with SPCM. The dashed white line indicates the MoS₂ flake boundary. Figure 4b shows the corresponding map of photocurrent acquired at $V_D = V_G = 0$ V, and Figure 4c contains the line profiles of the photocurrent at various drain biases. The fact that the photocurrent maximum traces the MoS₂ flake boundary in Figure 4b indicates that the photovoltage measured in Figure 3 arises from the pentacene/MoS₂ junction and not from built-in fields at the Schottky contacts. In addition, the photocurrent originating from the metal–pentacene junction, which becomes significant at positive

drain biases (Figure 4c), is of the opposite sign and therefore counteracts the photocurrent from the junction. Therefore, the V_{OC} measured in Figure 3 is likely reduced by the close proximity of the pentacene/MoS₂ junction to the non-Ohmic contact. Figure 4d shows a schematic of the simulated device geometry. Band-bending, which indicates the presence of electric fields that separate photogenerated charge carriers, is observed in the simulated band diagrams ($V_D = 0$ V) in both the vertical and horizontal directions (Figure 4e–f). The flat band condition occurs near $V_D = 0.6$ V (Figure 4g), in agreement with our experimental observation of zero photocurrent at the heterojunction near that biasing condition (Figure 4c, green curve), indicating that the V_{OC} could reach 0.6 V for ideal contacts.

Furthermore, the SPCM results reveal that I_{SC} from pentacene/MoS₂ heterojunctions could also be substantially improved by modifying the geometry to increase the carrier collection efficiency. While carriers generated near the edge of the MoS₂ flake are collected in the present device geometry, there is minimal photocurrent signal generated by the rest of the overlapped pentacene/MoS₂ heterojunction area for two reasons. First, excess carriers generated far from the edge of the pentacene/MoS₂ heterojunction area only experience a vertical electric field and must diffuse toward the contacts, while carriers generated at the edge of the flake experience a lateral

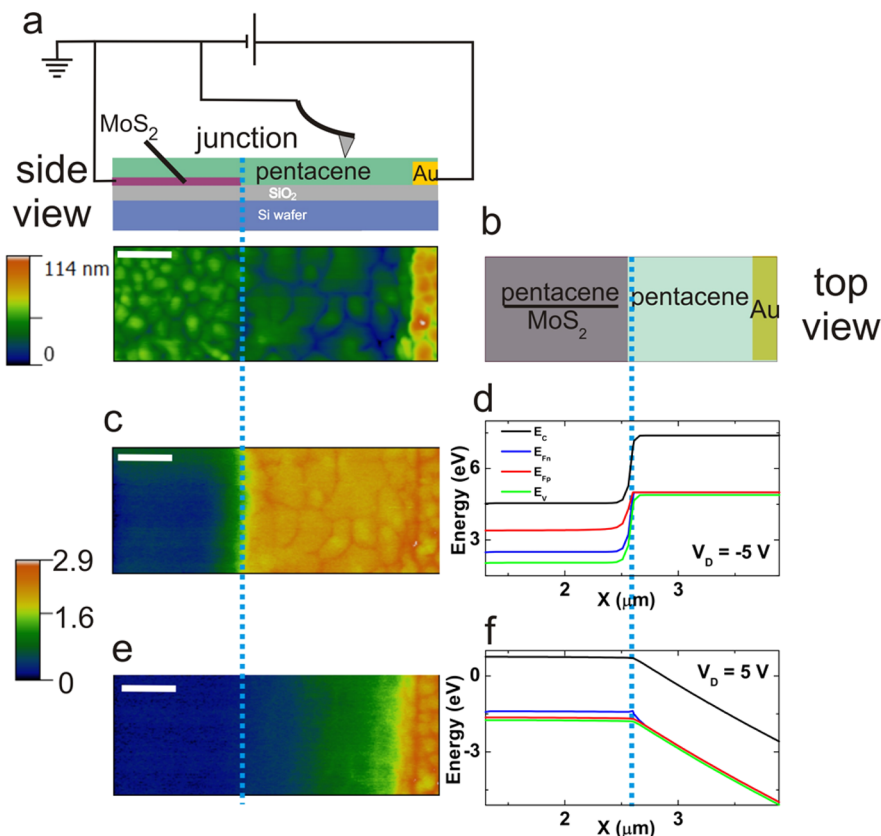


Figure 5. Electrostatic force microscopy. (a) Schematic side view of the measurement setup and device (top) with an AFM topography image of the device in Figure 1 with 2L MoS₂/40 nm pentacene (bottom). (b) Top view of the device with the labeled regions. (c) EFM phase map of the region shown in a at $V_D = -5$ V. (d) Corresponding simulated band diagram at the surface showing the potential drop at the edge of the overlapped pentacene/MoS₂ region. (e) EFM phase map of the region shown in a at $V_D = 5$ V. (f) Corresponding simulated band profiles at the surface showing a gradual potential drop across the pentacene channel (scale bar = 500 nm). The dashed blue line indicates the edge of the overlapped pentacene/MoS₂ region.

electric field that can drive them toward the contacts. Second, carriers generated in the overlapped pentacene/MoS₂ region likely have a much lower minority carrier diffusion length, $L_D = (\mu k_B T)^{0.5}$ where μ is the carrier mobility, τ is the carrier lifetime, k_B is the Boltzmann constant, and T is the temperature. As pointed out earlier in Figure 1d, the grain size of the pentacene is smaller on MoS₂ than on the surrounding SiO₂, which increases charge carrier scattering and trapping, resulting in lower values for μ and τ .^{29–31} A small L_D combined with a lateral geometry for charge collection thus minimizes the collection of charge carriers from the overlapped region. Consistent with organic photovoltaics, these results suggest that a vertical bulk heterojunction geometry would enable improved pentacene/MoS₂ photovoltaic device metrics.

While photocurrent is not observed throughout the overlapped pentacene/MoS₂ region, the above discussion and modeling indicates that a vertical built-in field is still present. To confirm the existence of this vertical electric field, we performed surface potential measurements using electrostatic force microscopy (EFM). EFM records both the sample topography and the phase shift of the cantilever vibration resulting from electrostatic force gradients (Figure 5a,b; Supporting Information, Figure S3). The shifted phase angle color maps shown in Figures 5c and e are proportional to $(V_{\text{tip}} - V_{\text{sample}})^2$, where V_{tip} is the tip bias and V_{sample} is the sample surface potential, which varies with electrode biasing conditions. Under a large reverse bias (Figure 5c), there is a sharp potential drop at the end of

the MoS₂ flake, and the surface potential is flat in other parts of the device channel, in agreement with the corresponding simulated band profile in Figure 5d. At large forward bias (Figure 5e), the junction is no longer the most resistive part of the circuit. Rather, the pentacene on SiO₂ acts as a current-limiting series resistor, resulting in a gradual drop in potential across the pentacene channel, again corroborated by the corresponding simulated profile (Figure 5f). The above surface potential profiles reveal that the underlying MoS₂ depletes the entire 2D junction area under reverse bias. While lateral charge transport is required in these devices based on the position of the electrodes, EFM provides direct evidence of band bending in the vertical direction over the entire overlapped pentacene/MoS₂ junction region, which could be exploited for carrier separation in vertically oriented photovoltaics.

In conclusion, we have fabricated and characterized an organic/2D semiconductor van der Waals p–n heterojunction using pentacene and MoS₂. The atomically thin MoS₂ allows the junction to be gate-tunable with an asymmetric antiambipolar transfer characteristic. Spatial photocurrent mapping and surface potential profiles combined with finite element simulations confirm band bending in both the lateral and vertical directions and a type-II band alignment. The observation of a photovoltaic effect implies that MoS₂ could be an alternative nonfullerene acceptor for organic photovoltaics and other hybrid bulk heterojunction solar cells. Considering that optimized single-junction pentacene/C₆₀ cells reported in the literature have

$V_{OC} \leq 0.4$ V,^{32,33} the results presented here are encouraging, especially considering the lateral device geometry and absence of any interfacial layers. While this study demonstrates the concept of an organic-2D MoS₂ hybrid photovoltaic device, semiconducting polymers could offer higher performance in large-area devices. With the availability of a library of organic molecules and polymers^{34,35} and solution processed³⁶ as well as chemical vapor deposited³⁷ ultrathin transition metal dichalcogenides, the concepts presented here can likely be scaled up to achieve high-performance organic/2D semiconductor van der Waals heterojunctions for use in gate-tunable diodes, hybrid photovoltaic devices, and related electronic and optoelectronic technologies.

Methods. Materials Synthesis and Deposition. MoS₂ flakes were deposited on 300 nm SiO₂/Si substrates via mechanical exfoliation of bulk crystals (SPI supplies). The resulting MoS₂ flakes were identified by optical microscopy and later characterized by Raman spectroscopy to determine the flake thickness (*Supporting Information*, Section S1). Pentacene powder was purchased from Sigma-Aldrich and purified further by multiple sublimation/deposition cycles under reduced pressure in a thermal gradient sublimation module (*Supporting Information*, Section S1). Next, 50 mg of the purified pentacene powder was loaded into a tungsten boat and placed in a thermal evaporator. The pentacene deposition was carried out in vacuum at a pressure $<5.0 \times 10^{-5}$ Torr at a rate of 0.1–0.2 Å/s. The substrate holder was not rotated and was maintained at room temperature throughout the deposition.

Device Fabrication and Electrical Measurements. Devices were fabricated using standard electron beam lithography (EBL) and thermal metal evaporation. In the second step of lithography, a window was opened atop the junction area using EBL, and a shadow mask (1 mm × 1 mm square) was used to limit the evaporated pentacene area. All electrical measurements were performed under high vacuum ($P < 5 \times 10^{-5}$ Torr) in a Lake Shore CRX 4K probe station using Keithley 2400 source meters and custom LabView programs (see *Supporting Information*, Sections S1 and S2 for more details).

Simulations. Sentaurus TCAD was used to model 2D devices by numerically solving the steady-state Poisson and continuity equations that govern free carrier transport using the finite element method. When available, the materials parameters in the simulations were taken from the literature. Other parameters were constrained by experimental measurements on uniform control FETs. Transport through the semiconductor junction was modeled by thermionic emission, and the contacts were modeled as Schottky barriers. Further simulation details can found in *Supporting Information*, Section S4.

■ ASSOCIATED CONTENT

● Supporting Information

The Supporting Information is available free of charge on the ACS Publications website at DOI: [10.1021/acs.nanolett.5b04141](https://doi.org/10.1021/acs.nanolett.5b04141).

Additional details on fabrication, electrical characterization, and simulations ([PDF](#))

■ AUTHOR INFORMATION

Corresponding Authors

*E-mail: m-hersam@northwestern.edu.

*E-mail: lauhon@northwestern.edu.

*E-mail: t-marks@northwestern.edu.

Author Contributions

D.J. and S.L.H. contributed equally.

Notes

The authors declare no competing financial interest.

■ ACKNOWLEDGMENTS

This research was supported by the Materials Research Science and Engineering Center (MRSEC) of Northwestern University (NSF DMR-1121262), and the 2-DARE program (NSF EFRI-143510). D.J. acknowledges additional support from an SPIE education scholarship and IEEE DEIS fellowship. This work made use of the Northwestern University Atomic and Nanoscale Characterization Experimental Center (NUANCE), which has received support from the NSF MRSEC (DMR-1121262), State of Illinois, and Northwestern University. In addition, the Raman instrumentation was funded by the Argonne-Northwestern Solar Energy Research (ANSER) Energy Frontier Research Center (DOE DE-SC0001059). The authors thank A. Walker, K. Stallings, and S. Clark for advice and assistance with pentacene deposition processes as well as J. Kang for help with the optical absorbance measurements.

■ REFERENCES

- (1) Grigorieva, I. V.; Geim, A. K. *Nature* **2013**, *499*, 419–425.
- (2) Jariwala, D.; Sangwan, V. K.; Lauhon, L. J.; Marks, T. J.; Hersam, M. C. *ACS Nano* **2014**, *8*, 1102–1120.
- (3) Britnell, L.; Gorbachev, R. V.; Jalil, R.; Belle, B. D.; Schedin, F.; Mishchenko, A.; Georgiou, T.; Katsnelson, M. I.; Eaves, L.; Morozov, S. V.; Peres, N. M. R.; Leist, J.; Geim, A. K.; Novoselov, K. S.; Ponomarenko, L. A. *Science* **2012**, *335*, 947–950.
- (4) Britnell, L.; Ribeiro, R.; Eckmann, A.; Jalil, R.; Belle, B.; Mishchenko, A.; Kim, Y.-J.; Gorbachev, R.; Georgiou, T.; Morozov, S.; Grigorenko, A.; Geim, A. K.; Casiraghi, C.; Castro-Neto, A.; Novoselov, K. S. *Science* **2013**, *340*, 1311–1314.
- (5) Georgiou, T.; Jalil, R.; Belle, B. D.; Britnell, L.; Gorbachev, R. V.; Morozov, S. V.; Kim, Y.-J.; Ghosh, A.; Haigh, S. J.; Makarovsky, O.; Eaves, L.; Ponomarenko, L. A.; Geim, A. K.; Novoselov, K. S.; Mishchenko, A. *Nat. Nanotechnol.* **2012**, *8*, 100–103.
- (6) Choi, M. S.; Lee, G.-H.; Yu, Y.-J.; Lee, D.-Y.; Lee, S. H.; Kim, P.; Hone, J.; Yoo, W. J. *Nat. Commun.* **2013**, *4*, 1624.
- (7) Esmaeili-Rad, M. R.; Salahuddin, S. *Sci. Rep.* **2013**, *3*, 2345.
- (8) Ye, Y.; Ye, Z.; Ghosh, A.; Zhu, H.; Zhao, M.; Wang, Y.; Yin, X.; Zhang, X. *Appl. Phys. Lett.* **2014**, *104*, 193508.
- (9) Yang, H.; Heo, J.; Park, S.; Song, H. J.; Seo, D. H.; Byun, K.-E.; Kim, P.; Yoo, I.; Chung, H.-J.; Kim, K. *Science* **2012**, *336*, 1140–1143.
- (10) Jariwala, D.; Sangwan, V. K.; Wu, C.-C.; Prabhakar, P. L.; Geier, M. L.; Marks, T. J.; Lauhon, L. J.; Hersam, M. C. *Proc. Natl. Acad. Sci. U. S. A.* **2013**, *110*, 18076–18080.
- (11) Jariwala, D.; Sangwan, V. K.; Seo, J.-W. T.; Xu, W.; Smith, J.; Kim, C. H.; Lauhon, L. J.; Marks, T. J.; Hersam, M. C. *Nano Lett.* **2015**, *15*, 416–421.
- (12) Lee, G.-H.; Lee, C.-H.; van der Zande, A. M.; Han, M.; Cui, X.; Arefe, G.; Nuckolls, C.; Heinz, T. F.; Hone, J.; Kim, P. *APL Mater.* **2014**, *2*, 092511.
- (13) Kang, S. J.; Lee, G.-H.; Yu, Y.-J.; Zhao, Y.; Kim, B.; Watanabe, K.; Taniguchi, T.; Hone, J.; Kim, P.; Nuckolls, C. *Adv. Funct. Mater.* **2014**, *24*, 5157–5163.
- (14) Lee, C.-H.; Schiros, T.; Santos, E. J. G.; Kim, B.; Yager, K. G.; Kang, S. J.; Lee, S.; Yu, J.; Watanabe, K.; Taniguchi, T.; Hone, J.; Kaxiras, E.; Nuckolls, C.; Kim, P. *Adv. Mater.* **2014**, *26*, 2812–2817.
- (15) He, D.; Zhang, Y.; Wu, Q.; Xu, R.; Nan, H.; Liu, J.; Yao, J.; Wang, Z.; Yuan, S.; Li, Y.; Shi, Y.; Wang, J.; Ni, Z.; He, L.; Miao, F.; Song, F.; Xu, H.; Watanabe, K.; Taniguchi, T.; Xu, J.-B.; Wang, X. *Nat. Commun.* **2014**, *5*, 5162.

- (16) Lee, W. H.; Park, J.; Sim, S. H.; Lim, S.; Kim, K. S.; Hong, B. H.; Cho, K. *J. Am. Chem. Soc.* **2011**, *133*, 4447–4454.
- (17) Velez, S.; Ciudad, D.; Island, J.; Buscema, M.; Txoperena, O.; Parui, S.; Steele, G. A.; Casanova, F.; van der Zant, H. S. J.; Castellanos-Gomez, A.; Hueso, L. *Nanoscale* **2015**, *7*, 15442–15449.
- (18) Liu, F.; Chow, W. L.; He, X.; Hu, P.; Zheng, S.; Wang, X.; Zhou, J.; Fu, Q.; Fu, W.; Yu, P.; Zeng, Q.; Fan, H. J.; Tay, B. K.; Kloc, C.; Liu, Z. *Adv. Funct. Mater.* **2015**, *25*, 5865–5871.
- (19) Han, W.; Yoshida, H.; Ueno, N.; Kera, S. *Appl. Phys. Lett.* **2013**, *103*, 123303.
- (20) Schlaf, R.; Lang, O.; Pettenkofer, C.; Jaegermann, W. *J. Appl. Phys.* **1999**, *85*, 2732–2753.
- (21) Howell, S. L.; Jariwala, D.; Wu, C.-C.; Chen, K.-S.; Sangwan, V. K.; Kang, J.; Marks, T. J.; Hersam, M. C.; Lauhon, L. J. *Nano Lett.* **2015**, *15*, 2278–2284.
- (22) Furchi, M. M.; Pospischil, A.; Libisch, F.; Burgdörfer, J.; Mueller, T. *Nano Lett.* **2014**, *14*, 4785–4791.
- (23) Lee, C.-H.; Lee, G.-H.; van der Zande, A. M.; Chen, W.; Li, Y.; Han, M.; Cui, X.; Arefe, G.; Nuckolls, C.; Heinz, T. F.; Guo, J.; Hone, J.; Kim, P. *Nat. Nanotechnol.* **2014**, *9*, 676–681.
- (24) Xiong, F. Amplitude Shift Keying. In *Encyclopedia of RF and Microwave Engineering*; John Wiley & Sons, Inc., 2005.
- (25) Chhikara, M.; Pavlica, E.; Bratina, G. *Surf. Sci.* **2013**, *609*, L5–L8.
- (26) Kim, K.; Santos, E. J. G.; Lee, T. H.; Nishi, Y.; Bao, Z. *Small* **2015**, *11*, 2037–2043.
- (27) Castellanos-Gomez, A.; Agrait, N.; Rubio-Bollinger, G. *Appl. Phys. Lett.* **2010**, *96*, 213116.
- (28) Tiago, M. L.; Northrup, J. E.; Louie, S. G. *Phys. Rev. B: Condens. Matter Mater. Phys.* **2003**, *67*, 115212.
- (29) Horowitz, G.; Hajlaoui, M. E. *Synth. Met.* **2001**, *122*, 185–189.
- (30) Bolognesi, A.; Berliocchi, M.; Manenti, M.; Di Carlo, A.; Lugli, P.; Lmimouni, K.; Dufour, C. *IEEE Trans. Electron Devices* **2004**, *51*, 1997–2003.
- (31) Street, R. A.; Knipp, D.; Völkel, A. R. *Appl. Phys. Lett.* **2002**, *80*, 1658–1660.
- (32) Yang, J.; Nguyen, T.-Q. *Org. Electron.* **2007**, *8*, 566–574.
- (33) Cheyns, D.; Gommans, H.; Odijk, M.; Poortmans, J.; Heremans, P. *Sol. Energy Mater. Sol. Cells* **2007**, *91*, 399–404.
- (34) Marks, T. J. *MRS Bull.* **2010**, *35*, 1018–1027.
- (35) Kroon, R.; Lenes, M.; Hummelen, J. C.; Blom, P. W. M.; de Boer, B. *Polym. Rev.* **2008**, *48*, 531–582.
- (36) Kang, J.; Seo, J.-W. T.; Alducin, D.; Ponce, A.; Yacaman, M. J.; Hersam, M. C. *Nat. Commun.* **2014**, *5*, 5478.
- (37) Kang, K.; Xie, S.; Huang, L.; Han, Y.; Huang, P. Y.; Mak, K. F.; Kim, C.-J.; Muller, D.; Park, J. *Nature* **2015**, *520*, 656–660.